Polarized angular-dependent reflectivity and density-dependent profiles of shock-compressed xenon plasmas

Y. Zaporozhets, V. Mintsev, and V. Fortov
Institute of Problems of Chemical Physics, Chernogolovka, Moscow Reg., 142432 Russia

H. Reinholz
University of Western Australia, School of Physics, 35 Stirling Highway, Crawley, Western Australia 6009, Australia and University of Rostock, Institute of Physics, Universitätsplatz 1, D-18051 Rostock, Germany

G. Röpke
University of Rostock, Institute of Physics, Universitätsplatz 1, D-18051 Rostock, Germany

S. Rosmej
Carl von Ossietzky University of Oldenburg, Institute of Physics, D-26111 Oldenburg, Germany

Y. A. Omarbakiyeva
International IT University, 050040, Almaty, Kazakhstan

(Received 26 December 2018; published 3 April 2019)

New data for the reflectivity of shock-compressed xenon plasmas at pressures of 10–12 GPa at large incident angles are presented. In addition, measurements have been performed at different densities. These data allow to analyze the free-electron density profile across the shock wave front. Assuming a Fermi-like density profile, the width of the front layer is inferred. The reflectivity coefficients for the *s*- and *p*-polarized waves are calculated. The influence of atoms, which was taken into account on the level of the collision frequency, proves to be essential for the understanding of the reflection process. Subsequently, a unique density profile is sufficient to obtain good agreement with the experimental data at different incident angles and at all investigated optical laser frequencies. Reflectivity measurements for different densities allow to determine the dependence of shock-front density profiles on the plasma parameters. As a result, it was found that the width of the front layer increases with decreasing density.

DOI: 10.1103/PhysRevE.99.043202

I. INTRODUCTION

The optical conductivity is one of the most interesting properties of nonideal plasmas. In a warm dense matter regime, where the plasma is strongly coupled and degenerate, the transition from a low-conducting state to a state with high, metal-like conductivity is a phenomenon of fundamental relevance for many other physical properties. As one of those, reflectivity measurements on the surface of dense plasma, which are produced, e.g., by shock waves, are an important tool to investigate the state of such nonideal plasmas. For instance, a jump of the reflectivity in dense liquid hydrogen and deuterium was reported in Refs. [1–4] which has been interpreted as the transition to a conducting fluid state at high pressure. The position of a first-order phase transition to metallic hydrogen in the phase diagram obtained by these experiments has been discussed in recent publications, see Refs. [5–7].

In this work, we focus on experiments with shock-compressed Xe [8]. The determination of the conductivity as a signature for the ionization and the formation of a plasma state can be performed by the measurement of the reflectivity at the plasma front. The reflectivity was measured for different laser wave lengths, polarization, and incident angles [8–10]. A transition from a dielectric to a metal-like state occurs with increasing density due to pressure ionization [8,10–13]. Earlier we measured the reflectivity using radiation of a laser beam at fixed frequency $\nu_{\rm las}$. It was found, that the reflectivity was considerably lower than theoretically expected. This indicates that the collisionless plasma model described by the random phase approximation (RPA) is not valid.

A theoretical analysis of the reflectivity data of a xenon plasma under normal incidence has been performed in several earlier works. Berkovsky *et al.* [14,15] used a dielectric function in Born approximation. In Ref. [16], nonequilibrium effects were included and the level of a two-moment model for the electrical conductivity [17,18]. The density functional theory was utilized in Refs. [19–22]. In none of these works a consistent description of the measured reflectivity has been achieved and the reflectivity was overestimated by a factor of $\geqslant 2$, especially at low pressures.

Within these first attempts to analyze reflectivity measurements, the Fresnel formulas was utilized for the reflection at a plane interface, where the dielectric function jumps from a value ϵ_1 to ϵ_2. For different polarizations (s and p) of the light, wavelength $\lambda = c/\omega$, incident angle θ_0, the reflectivities

$\mathcal{R}_s$ and $\mathcal{R}_p$ were calculated as given below in Sec. III B. Of interest is the occurrence of a minimum of $\mathcal{R}_p$ at the Brewster angle. Furthermore, different frequencies ω of the incident laser light are accounted for by a frequency-dependent dielectric function $\epsilon(\omega; z)$ where z denotes the coordinate perpendicular to the shock-wave front. For the determination of the dielectric function, which was considered to be the main issue, different approaches were applied. However, it was not possible to explain the measured data, in particular, the dependence on the incident angle and the value of the Brewster angle when applying the Fresnel formulas, despite the fact that the electrical conductivity of homogeneous dense plasmas can be described well if applying a consistent approach to the dielectric function. Therefore, the assumption of a steplike change of $\epsilon(\omega; z)$ as function of z was abandoned. A smooth change of $\epsilon(\omega; z)$ requires the solution of the Helmholtz equations instead of the Fresnel formulas. This gradual change of $\epsilon(\omega; z)$ may be related to the free-electron density profile of the shock front, $n_e(z)$. It has been found [9,12,23–25] that in this way the measured data, in particular the angular and frequency dependence of the reflectivity, can be understood.

In this paper, we report results of s- and p-polarized reflectivity measurements of nonideal Xe plasma at $\nu_{las} = 2.83 \times 10^{14}$ s^{-1} ($\lambda = 1064$ nm), $\nu_{las} = 4.33 \times 10^{14}$ s^{-1} ($\lambda = 694$ nm), and $\nu_{las} = 5.66 \times 10^{14}$ s^{-1} ($\lambda = 532$ nm) and at incident angles of up to $\theta = 78$ degrees. The analysis of the measured reflectivity data allows to infer the profile of the shock wave front, i.e., the dependence $\epsilon(z)$. As a new aspect, different densities are considered to investigate the density dependence of the width of the shock-front layer.

The profile $\epsilon(z)$ across the shock front or, correspondingly, the complex conductivity $\sigma(z) = (i\omega\epsilon_0)[1 - \epsilon(z)]$ essentially depends on the free-electron density $n_e(z)$. We show that, with this assumption, the free-electron density profile is inferred. For this goal a well established and consistent theory of the conductivity in dense plasmas is applied. It considers a partially ionized gas where the ionization degree determines the free-electron density. Results for the conductivity of partially ionized plasmas are obtained from linear response theory [26]. The dynamical collision frequency contains the contribution of electron-ion, electron-electron, as well as electron-atom collisions, where recently new results have been achieved [27,28].

We present new experimental results for the wavelength and incident angle-dependent reflectivity in Sec. II. Also different densities are investigated. The discussion in Sec. III shows that ionization kinetics has to be taken into account to explain the free-electron density profile across the shock front. In contrast, a detailed measurement of the reflectivity as a function of incident angle, laser frequency, and polarization direction, shown in Sec. IV, allows to analyze microscopic processes such as ionization kinetics within a dense plasma environment.

II. EXPERIMENTAL SETUP

The measurements on plasma reflectivity were performed using inclined incidence of polarized electromagnetic waves at moderate intensity. The experimental setup is shown in Fig. 1.

To generate a nonideal plasma, we used explosively driven shock waves which lead to compression and irreversible heating of xenon. This hydrodynamic method makes it possible to obtain a well-reproducible plasma of sufficient size in the direction of probing, without undesirable electromagnetic fields, which would uncontrollably disturb the high-conducting plasma. The flatness and homogeneity of the plasma region were checked using an optical camera via transparent side walls of the gas cell. Extremely strong intrinsic thermal emission of the plasma requires the use of the pulse probe method. Using a computer-controlled laser system, the polarized reflectivity coefficient of dense xenon plasmas was determined with a four-channel pulse high-speed photodetector system. It allows to measure the intensity of the reflected laser beam for four azimuthal angles and was equipped with filters for the selection of the probing frequency. In Fig. 2, a typical signal of the probe pulse and the signal of one of the four photodetectors are marked in cyan and red, respectively. The probe pulse is shifted vertically for better presentation. The ratios of the amplitudes of the probe pulse and the signals of the four channels of the photodetector system are used to calculate the components of the Stokes vector.

In experiments at high angles of incidence, there is a substantial loss of the reflected radiation due to partial cutoff inside the gas cell. Additional measurements of the angular distribution of the energy reflected from the plasma at normal incidence, see Fig. 3, were carried out to correct the observed signals at tilted incidence. Also, based on these data, new gas cells have been constructed, see Figs. 4 and 5, for measurements at high incident angles. The forming and receiving aspherical lenses (called axicon) are oriented towards the bottom plane of the cell so that they provide optimal conditions for collecting the reflected laser light. In our experiments, either aspherical lenses and fiber optics have been used. The results are in good agreement. However, with aspherical lenses dynamic errors are smaller. The design also allows to vary the material for the bottom of the gas cells. The best results were obtained using polished tungsten. The gas cells have a thermostating system to stabilize the initial temperature and density of the gas under study. In addition, the cell is equipped with a vacuuming and gas supply system and has photoelectric and ionization sensors to monitor the position of the shock wave front.

Experimental data for the reflectivity are obtained for different frequencies using a pulsed $Y_3Al_5O_{12}$:Nd^{3+} laser. The laser wavelengths $\lambda = c/\nu_{las}$ and the conditions of the initial and final xenon gas are shown in Table I. The experiments were performed starting off with an uncompressed neutral gas of two different mass densities ρ_0 and initial pressure P_0 at room temperature $T_0 = 294$ K. Thermodynamic and plasma parameters are given, such as pressure P, temperature T, mass density ρ, free electron density n_e, density of neutral atoms n_a, and the ionization degree $\alpha_{ion} = n_e/(n_a + n_e)$ of the shock wave produced plasma. Whereas the final temperature is nearly the same (3×10^4 K), the densities differ depending on the initial gas density. The measurements at mass density 2.8 g/cm^3 are performed at three different frequencies of the probe laser. The plasma is strongly coupled as indicated by the

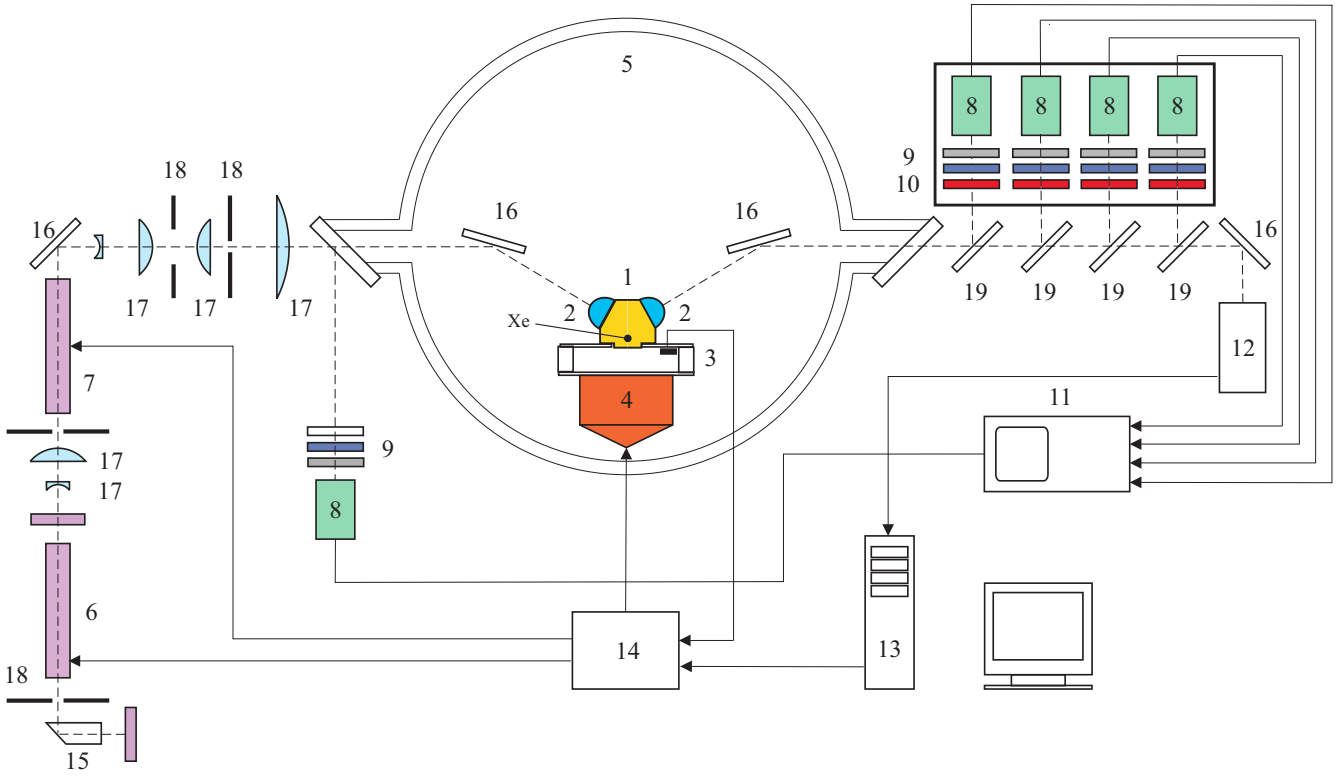

FIG. 1. Experimental setup: 1 - gas cell with 2 - axicon, 3 - sensor for measuring the speed of the striker, 4 - explosively driven shock wave generator, 5 - experimental chamber with observation windows, 6 - laser, 7 - laser amplifier, 8 - photodetector with 9 - interference filter and 10 - polarizer, 11- digitizing oscilloscope, 12 - spectroscope, 13 - control computer, 14 - high speed control block, and various optical components: 15 - $KTiOPO_4$ crystal, 16 - dielectric mirror, 17 - lens, 18 - diaphragm, 19 - laser beam splitter.

nonideality parameter $\Gamma = e^2/(4\pi\epsilon_0 k_B T) \times (4\pi n_e^{pl}/3)^{1/3} > 1$. The degeneracy parameter $\Theta = 2mk_B T/\hbar^2 \times (3\pi^2 n_e^{pl})^{-2/3}$ is close to unity so that we are in the warm dense matter (WDM) region.

The thermodynamic parameters of the plasma including the composition were determined for given shock velocities, as measured in the experiment, using the method of minimization of the free energy [29]. Short-range repulsion of atoms and ions as well as the Coulomb interaction of charged particles have been taken into account. For the last of these, screening was treated via the summation of ring diagrams (Debye approximation) for the viral corrections within a grand canonical ensemble for multiple ionization.

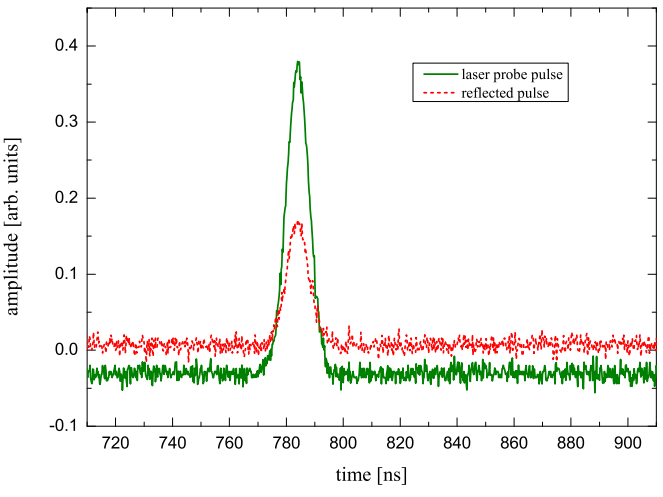

FIG. 2. A representative oscillogram showing the amplitude of the probe pulse and a typical signal of one of the four channels of the photodetector system.

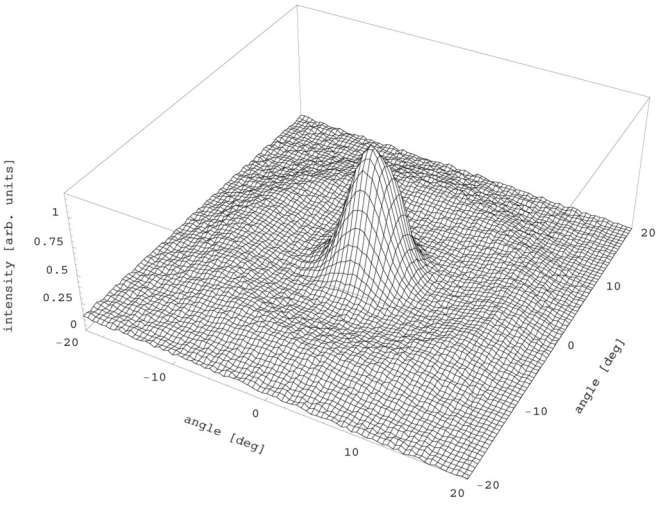

FIG. 3. The angular energy distribution of the reflected light for normal incidence and probing laser of $\lambda = 694$ nm. The angles relative to the normal are given in the x-y plane which is perpendicular to the normal.

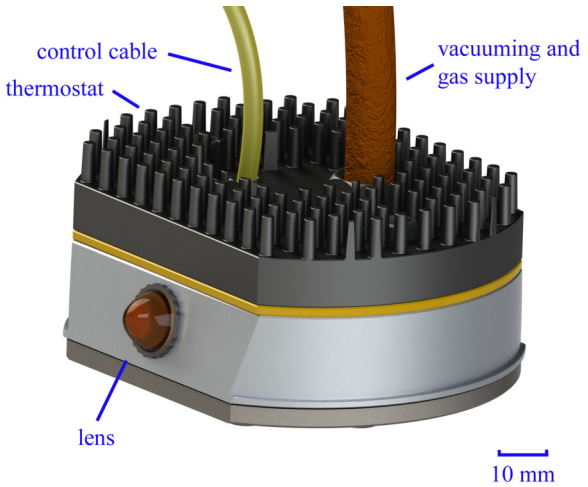

FIG. 4. Gas cell with aspherical lenses (axicon) for measurements at large incident angles. Only the lens for the incoming probe pulse is visible.

Short-range repulsion of heavy particles was considered within the framework of a soft sphere model. In the parameter range of the shock wave experiments, the composition was obtained with an error of up to 15%, depending on the approximations for the equation of state. For further details on the SAHA IV code by Gryaznov *et al.* see Refs. [29–32]. Experimental measurements of the plasma temperature by a three-channel pyrometer was performed in several experiments. A reasonable agreement with the calculated values was obtained, with differences of no more than 10–15%. Finally, the experimental data for s- and p-polarized reflectivities $\mathcal{R}_s$, $\mathcal{R}_p$ of explosively driven dense xenon plasma at different laser wavelengths are shown in Table II.

III. DENSITY PROFILE AT THE PLASMA FRONT

A. Dielectric function

The reflectivity of laser light with frequency $\omega = 2\pi c/\lambda$ on Xe plasma can be derived from the solution of the Maxwell

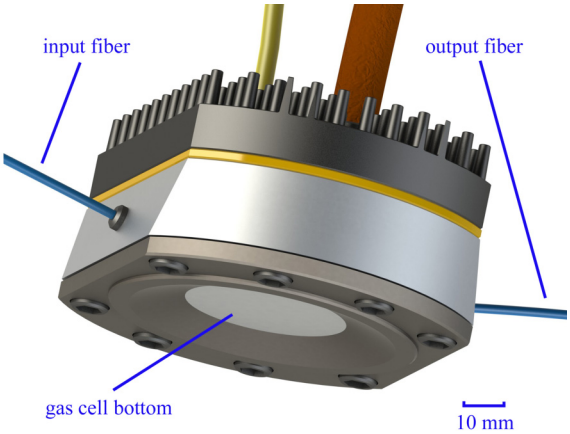

FIG. 5. Gas cell with optic fibers for measurements at large incident angles. The tungsten bottom of the gas cell is clearly visible.

equations. The dependence on the reflecting material enters via the dielectric function of xenon $\epsilon(n_e, T; \mathbf{q}, \omega)$. Here the wavelength λ can be considered at being large compared to the atomic scale. Therefore, we work in the long wavelength limit ($\mathbf{q} = 0$). The free-electron density n_e and the temperature T define the local thermodynamic equilibrium state for which the dielectric function is considered.

As was shown before [9], it is necessary to go beyond a collisionless RPA approximation and consider collisional and screening effects within the plasma. For this, the dielectric function is expressed via a generalized Drude formula [33] (in the following, we drop the parameter n_e, T)

$$\epsilon(\omega) = 1 - \frac{\omega_{\rm pl}^2}{\omega}\frac{1}{\omega + i\nu(\omega)}, \tag{1}$$

where $\omega_{\rm pl} = [n_e e^2/\epsilon_0 m]^{1/2}$ is the plasma frequency. According to the Matthiessen rule, the total collision frequency $\nu[n_e(z), n_a(z), T, \omega]$ is the sum of the contributions owing to the different scattering processes, the electron-ion (ei) and the electron-atom (ea) collisions,

$$\nu(n_e, n_a, T, \omega) = \nu_{ei}(n_i, n_e, T, \omega) + \nu_{ea}(n_a, n_e, T, \omega). \tag{2}$$

Collisions due to electron-electron interactions could naturally be included in the approach, but are of negligible relevance for conditions considered here. It has also been shown [9] that the dependence on ω is only weak for laser frequencies much smaller than the plasma frequency. Therefore, for the frequencies considered here, we treat the collision frequencies in static approximation ($\omega = 0$).

In contrast to former calculations, the collision frequencies are now calculated within a consistent approach by going beyond Born approximation and treating the ea collisions on the same level as the ei collisions. Strong collisions are taken into account using a T-matrix approach. The static collision frequency in both (ei, ea) channels can be expressed as

$$\nu_{ec}(n_c, n_e, T, \omega = 0) = \frac{\beta}{n_e m}\frac{\hbar^3}{3\pi^2 m} n_c \int_0^\infty dk\, k^5 f_k^e \left(1 - f_k^e\right) Q_{\rm T}^{ec}(k), \tag{3}$$

introducing the momentum-transfer cross section $Q_{\rm T}^{ec}$ for collisions with both species $c = i, a$, ions, and atoms, respectively. There is an extended literature on the treatment of the electron-ion momentum-transfer cross section $Q_{\rm T}^{ei}$, see Refs. [34,35] and references given there. Here we use the results of Rosmej [34] to calculate the e–i contribution to the collision frequency. In previous papers [9,36], the contribution of the collisions with neutral Xe atoms was taken into account via a factor f as $\nu_{ea}(n_a, n_e, T, 0) = f \times \nu_{ei}(n_i, n_e, T, 0)$. A concise microscopic approach was derived by Rosmej *et al.* [28,37] and is now available to calculate the transport cross section for e–a collisions. Following Ref. [28], we use a Debye potential for the electron-ion and a screened optical potential for the electron-atom interaction. Note that, calculating transport properties within these approximations, good agreement with experimental results on the dc-conductivity of homogeneous xenon and other inert gases has been obtained.

Further improvements which might need to be considered are the account of e–e collisions as well as higher moments of the electron momentum distribution function. In the parameter

TABLE I. Parameters of the shock-compressed plasma.

		Initial xenon gas				Shock-compressed xenon plasma							
No.	λ [nm]	P_0 [MPa]	T_0 [K]	ρ_0 [g/cm^3]	n_0 [10^{21}/cm^3]	P [GPa]	T^{pl} [K]	ρ [g/cm^3]	n_e^{pl} [10^{21}/cm^3]	n_a^{pl} [10^{21}/cm^3]	α_{ion}	Γ	Θ
1	1064	2.8	294	0.18	0.83	7	32700	1.8	5.6	2.8	0.67	1.5	2.3
2	1064	4	294	0.29	1.3	10.5	29250	2.7	7.1	5.4	0.57	1.8	1.9
3	694	4	294	0.29	1.3	12	32020	2.8	7.8	5.0	0.61	1.7	1.9
4	532	4	294	0.29	1.3	12	32020	2.8	7.8	5.0	0.61	1.7	1.9

range considered here, these only lead to marginal effects. In the following we will discuss the shape of the plasma front.

B. Fresnel formula for steplike density profile

In the case of a homogeneous medium with a constant dielectric function ϵ, the solution of the Maxwell equations are plane waves. Considering two half-spaces with ϵ_1 and ϵ_2 and a plane interface in between, the light propagation is given by the Fresnel formulas. The dielectric function ϵ of the plasma 1 is determined by the composition of the plasma. If we assume a steplike profile for the density of free electrons, the Fresnel formulas can be applied to calculate the reflectivity at the plasma front depending on the incident angle θ and the polarization. For s-polarized (electric field is polarized perpendicular to the incident plane and to the propagation direction of the shock wave front) p-polarized electromagnetic waves, the reflectivity is given by the Fresnel formulas

$$\mathcal{R}_s = \left(\frac{|\sqrt{\epsilon_1}\cos\theta - \sqrt{\epsilon_2 - \epsilon_1 \sin^2\theta}|}{|\sqrt{\epsilon_1}\cos\theta + \sqrt{\epsilon_2 - \epsilon_1 \sin^2\theta}|} \right)^2 \tag{4}$$

TABLE II. Experimental data for reflectivity of s- and p-polarized light depending on incident angle θ. For laser wavelengths and plasma parameters see Table I.

No	1		2		3		4	
θ [°]	$\mathcal{R}_s$	$\mathcal{R}_p$	$\mathcal{R}_s$	$\mathcal{R}_p$	$\mathcal{R}_s$	$\mathcal{R}_p$	$\mathcal{R}_s$	$\mathcal{R}_p$
0	0.25	0.25	0.37	0.37	0.26	0.26	0.16	0.16
10	0.28	0.24	0.41	0.35	0.31	0.24	0.20	0.12
20	0.39	0.22	0.47	0.32	0.37	0.18	0.21	0.11
30	0.55	0.18	0.52	0.25	0.384	0.15	0.30	0.085
35	0.52	0.21	–	–	0.52	0.12	0.39	0.07
40	0.58	0.13	0.64	0.17	0.57	0.13	0.37	0.083
45	0.58	0.20	0.65	0.158	0.585	0.12	0.48	0.14
50	0.69	0.17	0.70	0.163	0.55	0.15	0.50	0.17
55	0.67	0.27	0.74	0.165	0.60	0.14	0.58	0.19
60	0.72	0.32	0.73	0.168	0.70	0.19	0.61	0.30
65	0.735	0.48	0.80	0.223	0.79	0.33	0.72	0.43
70			0.85	0.28	0.78	0.30	0.80	0.48
75			0.89	0.52	0.82	0.56	0.87	0.62
78			0.91	0.60	0.86	0.63	0.90	0.69

and

$$\mathcal{R}_p = \left(\frac{|\epsilon_2\cos\theta - \sqrt{\epsilon_1(\epsilon_2 - \epsilon_1 \sin^2\theta)}|}{|\epsilon_2\cos\theta + \sqrt{\epsilon_1(\epsilon_2 - \epsilon_1 \sin^2\theta)}|} \right)^2, \tag{5}$$

respectively. Of particular interest is the occurrence of a reflectivity minimum for the p-wave at the so-called Brewster angle θ_{B}. As will be discussed in Sec. IV, the use of the Fresnel formula does not allow to explain the experimental results satisfactorily.

C. Fermi-like density profiles

We expect that the shock wave produced plasma front is not homogeneous, but the ionization degree and therefore the composition increases gradually along the propagation direction z of the shock wave front. We use a comoving system where the front is located at $z = 0$. Thus, the free-electron density $n_e(z)$ and temperature $T(z)$ define the local thermodynamic equilibrium state to calculate the dielectric function, becoming parametrically dependent on z as well.

Mintsev *et al.* [8] suggested an electron density profile at the shock front consisting of three regions: a precursor zone starting from a low density of the uncompressed initial neutral gas, a shock front zone, and the final plasma zone. The precursor is determined by radiation heating [38], but will not be discussed in detail here. To fit such a structure, Raitza *et al.* [39] suggested a Fermi-like profile for the free-electron density across the shock wave front

$$n_e(z) = \frac{n_e^{\mathrm{pl}}}{1 + \exp\{-(z - z_0)/A - \exp[(z - z_0)/B]\}}, \tag{6}$$

where $A\,B$ and z_0 are fit parameters, n_e^{pl} is the free-electron density in the final plasma zone which was derived from the experiment, see Table I. We will define the width of the profile as the region where the free-electron density increases from 0.1 to 0.9 of its final value.

The profile for the heavy particle density $n_{\mathrm{heavy}}(z) = n_a(z) + n_i(z)$ will also be assumed as Fermi-like

$$n_{\mathrm{heavy}}(z) = n_0 + \frac{n_a^{\mathrm{pl}} + n_i^{\mathrm{pl}} - n_0}{1 + \exp\{-z/D\}}, \tag{7}$$

where D is a fit parameter which determines the width of the profile. In contrast to the free-electron density profile, we expect a more steplike behavior, thus $D \lesssim A$. Note that the fraction of neutral Xe atoms is reduced as the ion density increases, which is equal to the free-electron density because

TABLE III. Fitting parameters for density profiles, Eqs. (6) and (7). For laser wavelengths and more plasma parameters see Table I.

No	ρ_0 [g/cm^3]	ρ [g/cm^3]	A [μm]	B [μm]	z_0 [μm]	D [μm]
1	0.18	1.8	0.08	1.5	0.165	0.01
2	0.29	2.7	0.03	1.5	0.045	0.01
3,4	0.29	2.8	0.03	1.5	0.045	0.01

of charge neutrality. Particle in cell (PIC) simulations [40] find a narrowing of the shock wave front layer of the order of 10 a_B.

Besides the density profile, also a temperature profile across the plasma front has to be considered, as discussed by Zeldovich and Raizer [41] and in Sec. IV B below. For the dielectric function, the temperature dependence is weak. We performed calculations with $\epsilon[n_e(z), T(z); \mathbf{q}, \omega]$ at different T and found almost no effect. In view of these results, we assume a constant temperature $T(z) \approx T^{\rm pl}$, see Table I.

In general, the free-electron density should not be obtained from a Saha equation but is a nonequilibrium quantity which approaches its equilibrium value after a time interval characterized by ionization and/or recombination reaction rates. This will also be discussed in Sec. IV C.

IV. REFLECTIVITY OF Xe PLASMA

A. Results

The reflectivity for shock-wave produced Xe plasma has been calculated solving the Helmholtz equations

$$\frac{d^2E_0(z)}{dz^2} + \frac{\omega^2}{c^2}[\epsilon(\omega, z) - \sin^2\theta]E_0(z) = 0, \tag{8}$$

$$\frac{d^2H_0(z)}{dz^2} - \frac{d}{dz}[\ln\epsilon(\omega, z)]\frac{dH_0(z)}{dz} + \frac{\omega^2}{c^2}[\epsilon(\omega, z) - \sin^2\theta]H_0(z) = 0, \tag{9}$$

for the complex amplitude of the electric field $E_0(z)$ and magnetic field $H_0(z)$, respectively, at laser frequency $\omega = 2\pi\nu_{\rm las}$. For the spacial distribution of the dielectric function, the Fermi-like profiles Eqs. (6) and (7) for free-electron density and heavy particle density, respectively, have been used as outlined in Sec. III C. The collision frequencies are treated in a consistent microscopic approach, as outlined in Sec. III A. Varying the free parameters to fit the experimental results, see Table II, we obtain the following parameters for the Fermi-like profiles as given in Table III.

The free-electron density profile of the shock front is shown in Fig. 6. We infer density profiles dependent only on the thermodynamic parameters which work for all wavelengths. We introduce the width $d = z_2 - z_1$ of the plasma front layer as the distance between the position z where 10 % of the free-electron density, $n_e(z_1) = 0.1\, n_e^{\rm pl}$, and 90% of the free-electron density, $n_e(z_2) = 0.9\, n_e^{\rm pl}$ is obtained. It is marked with dotted lines in Fig. 6. For the plasma densities 7.8×10^{21}/cm^3 and 5.6×10^{21}/cm^3 follow $d = 0.130\,\mu$m, for follows 0.335 μm. For higher plasma densities, the plasma front width becomes narrower.

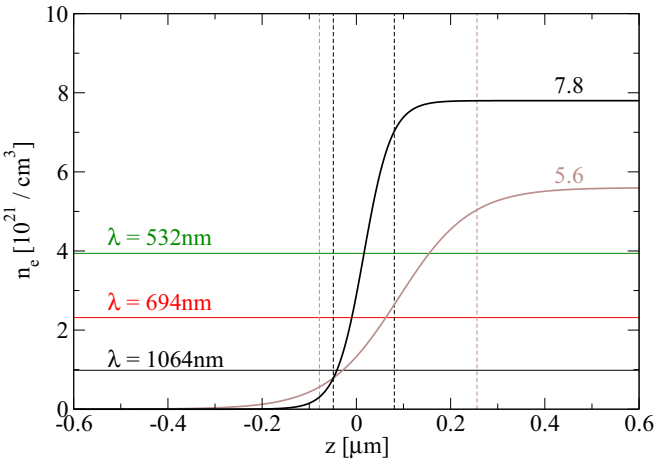

FIG. 6. Free-electron density profile (6) for free-electron density $n_e^{\rm pl} = 7.8 \times 10^{21}$ cm^{-3} and $n_e^{\rm pl} = 5.6 \times 10^{21}$ cm^{-3} in the plasma region. The critical electron densities are 0.987×10^{21} cm^{-3}, 2.32×10^{21} cm^{-3} and 3.95×10^{21} cm^{-3} for $\lambda_1 = 1064\,\mu$m, $\lambda_2 = 694\,\mu$m and $\lambda_3 = 532\,\mu$m, respectively. The width of the plasma front layer is marked with dotted lines.

The complete set of measured reflectivity data, see Table II, are shown in comparison to calculations in Figs. 7 and 8. Reasonable agreement with the experiments is observed for normal incidence ($\theta = 0$) as well as for other angles of incidence. In Fig. 7, we consider the reflectivity at wavelength $\lambda = 1064$ nm on plasma of densities $\rho = 1.8$ g/cm^3 and 2.7 g/cm^3. Figure 8 presents the reflectivity at different wavelengths $\lambda = 532$ and 694 nm on a plasma of the larger density $\rho = 2.8$ g/cm^3. The angular dependence of the s-wave reflectivity $\mathcal{R}_s$ is slightly underestimated. However, the Brewster angle, where the p-wave reflectivity $\mathcal{R}_p$ shows a minimum, is reproduced very well.

B. Discussion

The fact that the inferred density profiles only depend on the initial and final thermodynamic parameters but not on the laser frequency, see Table III, is a signature for the consistency of the suggested model. Note that it was not possible to reproduce the measurements at different wavelengths assuming the same steplike density profile for all wavelengths. It would be interesting, to make experiments at the lower density with additional wavelengths to further support the consistency of the free-electron density profile.

For a more detailed discussion of the approximations we show different approaches in Fig. 9, for the same parameters as shown in Fig. 8 left. For comparison, the reflectivity has been calculated for a steplike change of the dielectric function using the Fresnel formulas (4) and (5) for arbitrary incidence. If the dielectric function $\epsilon(\omega)$ takes into account only the e–i collisions, the reflectivity is significantly overestimated. Consideration of the e–a collisions reduces this discrepancy at least for normal incidence. Additional effects, as listed in Sec. III A, have also been considered here for comparison. In agreement with results in earlier papers, the account of e–e collisions as well as the account of higher moments of the electron momentum distribution function to calculate

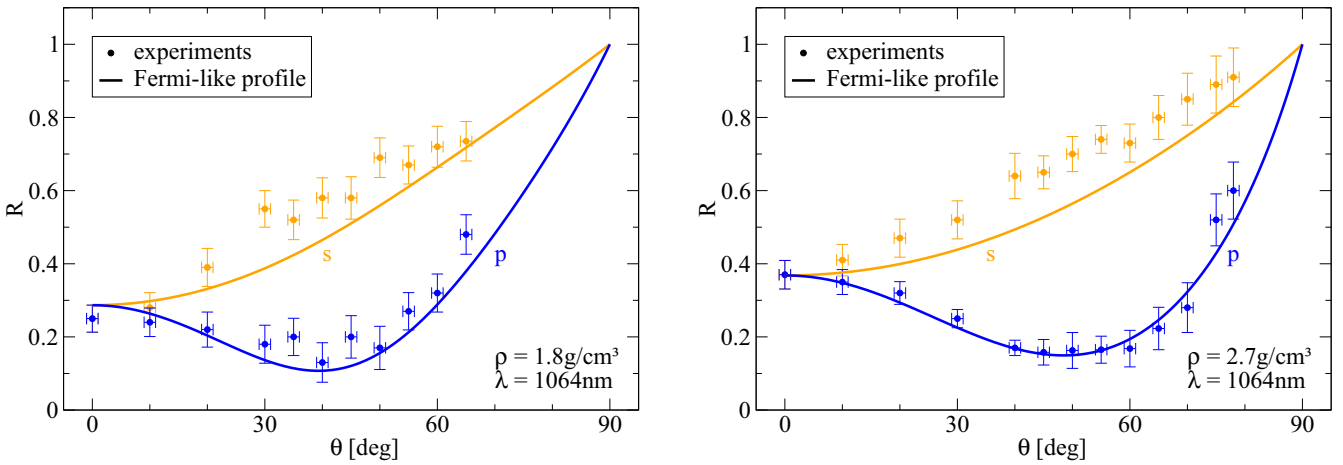

FIG. 7. Reflectivity calculated using Fermi-like profiles Eqs. (6) and (7) with parameters as given in Table III in comparison to experimental data, see Table II, for laser wavelength $\lambda = 1064$ nm on plasma of densities $\rho = 1.8$ and 2.7 g/cm^3; s polarization is orange, p polarization is blue.

$\epsilon(\omega)$ give only marginal effects. The frequency dependence of the collision frequency, leading to the occurrence of an imaginary part of the dielectric function, can also be neglected here, see Ref. [9]. More essential is the screening of the interaction within the plasma environment. We used an effective screening parameter for the e–i interaction and a screened optical potential for the e–a interaction. However, an improved calculation of the dielectric function will not resolve the discrepancy with the measured data at other than normal incidence.

In Fig. 10 the results of Norman *et al.* [22], obtained using a steplike density profile, are shown in comparison to this paper. Calculations have been done using quantum molecular dynamics (QMD) simulations, see also Ref. [21], which is largely similar to the simulation method in Ref. [19]. The main difference is that local field effects are taken into account and different pseudopotential models have been used. Again, reasonable agreement with the experiments is observed for normal incidence. This indicates that the model of a partially ionized plasma where the dielectric function contains contributions of free electrons as well as electrons bound in neutral clusters is appropriately chosen. However, the angular dependence of the reflectivity's $\mathcal{R}_p$, $\mathcal{R}_s$ is not well described using the MD simulations. In a subsequent paper by Norman *et al.* [23] a finite width of the front layer was assumed with a linear increase of the electron density. Slightly better agreement with experimental data has been obtained. Similar results were presented by Shalenov *et al.* [37], where the Fresnel formulas (4) and (5) were applied using a different set of effective interaction potentials for the calculation of the dielectric function in a similar approach as applied in this paper.

The Brewster angle, where $\mathcal{R}_p$ shows a minimum, should be considered since it is a specific property of a material. Figure 11 shows the Brewster angles obtained within different approaches as discussed before. We conclude that there are appropriate results for the dielectric function from the Green's function approach as well as from QMD simulations. The main problem is a nonequilibrium expression determined from a position-dependent ionization degree.

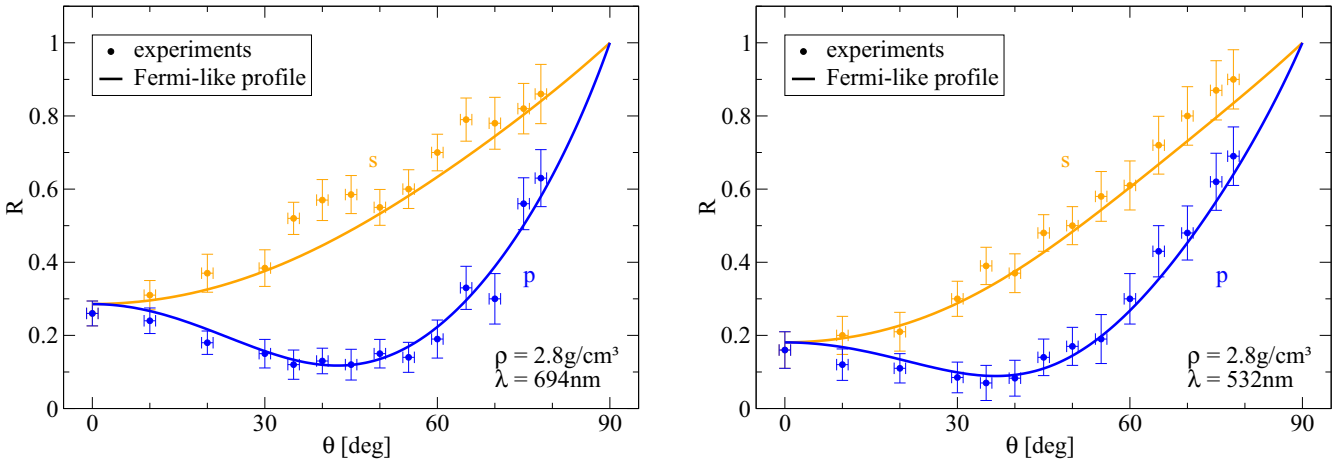

FIG. 8. Reflectivity calculated using Fermi-like profiles Eqs. (6) and (7) with parameters as given in Table III in comparison with experimental data, see Table II, for laser wavelength 694 and 532 nm on plasma of density $\rho = 2.8$ g/cm^3; s polarization is orange, p polarization is blue.

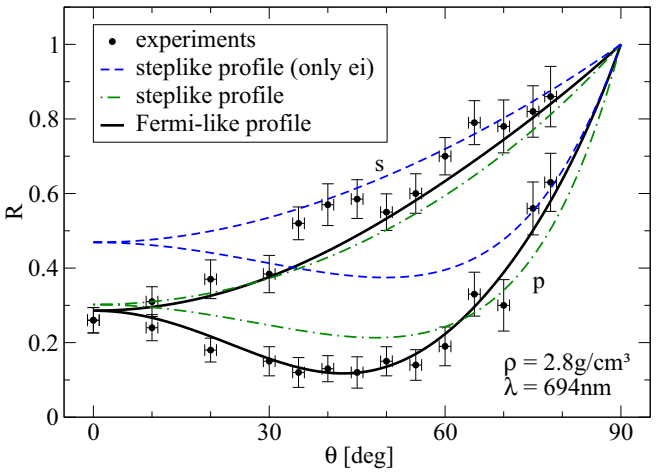

FIG. 9. Reflectivity results from Fig. 8 (black, full line) compared to calculations performed for steplike profiles including (green, dashed-dotted) and neglecting (blue, dashed) *e–a* collisions.

In conclusion, we can state, that considering a continuous, smooth profile of the free-electron density at the shock wave front when calculating the reflectivity, leads to results which are in overall good agreement for different incidence angles. The angular behavior, in particular the position of the Brewster angle, is better reproduced by calculations assuming a finite width of the front layer density profile.

An important issue is the assumption that the system is in local thermodynamic equilibrium. The ionization degree should be determined by a kinetic approach where the ionization rate is strongly depending on the plasma composition. The free electron subsystem has a very short relaxation time in the case considered here. A two-temperature description with an electron temperature T_e below the temperature T of the heavy particles would be more appropriate. In the plasma front layer, the ionization degree cannot be obtained from the Saha equation which is only valid for (local) thermodynamic equilibrium, but must be considered as a nonequilibrium quantity. Kubo-Greenwood expressions and similar approaches based on the fluctuation-dissipation theorem are not applicable be-

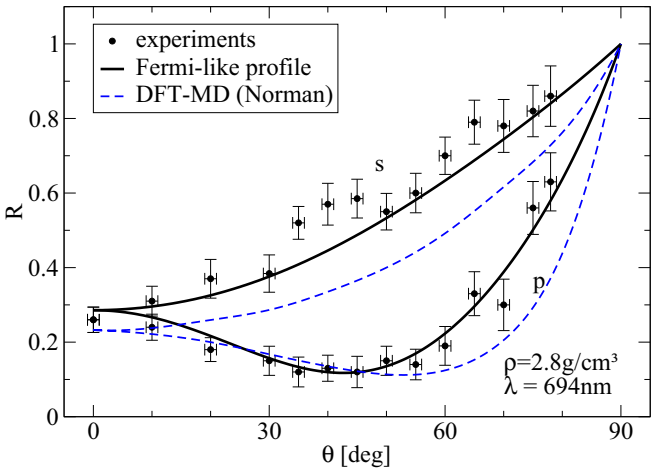

FIG. 10. Reflectivity results from Fig. 8 (black, full line) compared to DFT-MD simulations by Norman and Saitov [23] (blue, dashed).

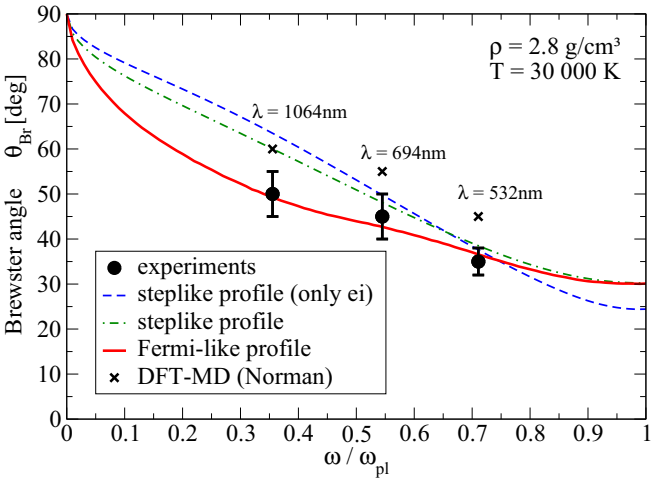

FIG. 11. Brewster angle for plasma of density $\rho = 2.8\,\mathrm{g/cm^3}$ in dependence on the frequency. Results performed with the Fermi-like profile Eq. (6) (red, full line) in comparison to experimental data (circles) and calculations performed for steplike profiles including (green, dashed-dotted) and neglecting (blue, dashed) *e–a* collisions as well as with DFT-MD simulations (**x**) by Norman and Saitov [23].

cause free electrons and electrons bound in atoms are not in full thermodynamic equilibrium. As a consequence, the experimental investigation of the properties of matter at high external energy input, based on the interaction of electromagnetic waves with plasma formation which is localized in space, always causes the need to study the characteristics of the boundary layer: the plasma layer, directly adjacent to the boundary of the "plasma-free space." This is of particular relevance in the case of dense shock-compressed plasma and will be addressed in the next subsection.

C. Ionization kinetics

To explain the free-electron density profile, Fig. 6, inferred from the analysis of reflectivity measurements, we discuss one of the relevant processes, the ionization kinetics. This last term describes the time evolution of the ionization degree within a chemical picture, where free electrons and electrons bound in neutral atoms are treated as different species. At lower densities ($n_e \approx 10^{17}/\mathrm{cm^3}$), the plasma front profile has been investigated [41–44]. The ionization rate is strongly dependent on the density of the plasma components. Near the WDM region, a strong enhancement due to in-medium effects (screening, ionization potential depression) is expected [45–47], so that the width of the plasma layer becomes narrower. Indeed, our reflectivity measurements give a clear indication for a finite width of the plasma transition layer. It is of interest to relate this to microscopic processes in the plasma. This refers also to former investigations of the propagation of the probing wave in the medium, studied both by hydrodynamic simulations, see, e.g., Ref. [40] and experiments on plasma reflectivity at different frequencies of the probe laser [9,10].

First-principle's microscopic calculations to derive the free-electron density profile of the shock front layer in the WDM region are complex and have not been performed until

now. PIC simulations of shock fronts by Diekmann *et al.* [40] only described the mass density profile, i.e., the density of particles not considering ionization. MD simulations [21] are not able to describe the motion of particles together with the reaction kinetics. For this, a quantum approach is necessary which describes free as well as bound state electrons. In addition, the microscopic processes occur on different time scales. The relaxation to local thermodynamical equilibrium within the electron subsystem is on the fs scale, whereas ionization processes occur on longer time scales.

At lower densities, ionization kinetics has been applied to describe the free-electron density profile of shock wave produced plasmas, see Ref. [42]. Different processes have been considered which lead to the equilibration of the ionization degree on a timescale of about 10^{-6} s. A strong dependence on the density of the shock-compressed gas is observed. A systematic description of the kinetics at the front of a shock wave has been given by Zeldovich and Raizer [41] and Biberman *et al.* [43]. For further details see Refs. [44,48–50], where shock waves at density $n_e \approx 10^{17}$ cm^{-3} and widths below 1 cm are described.

At densities typical for the WDM region, density effects such as screening, ionization potential depression [51], and Pauli blocking become of relevance in calculations of the impact ionization and three-body recombination coefficients [42,45–47]. As shown by Schlanges and Bornath [45], the ionization coefficient is increased by about a factor of 10 for the conditions considered here, if density effects are taken into account. As discussed by Wu *et al.* [47], the main influence of the plasma environment on impact ionization models is the continuum lowering and the corresponding lowering of the ionization energy.

The rate equation for bound states in dense many-particle systems has the form [45]

$$\frac{dn_a}{dt} = -\frac{dn_e}{dt} = \sum_c \{\beta_c n_i(t) n_e(t) n_c(t) - \alpha_c n_a(t) n_c(t)\}, \tag{10}$$

where the reaction $a \rightleftharpoons i + e$ under collisions with the components $c = \{e, i\}$ is considered, β_c and α_c are the recombination coefficient and ionization coefficient, respectively, due to collisions with species c. Both are related by detailed balance after equilibration, given by $\alpha_c/\beta_c = n_e^{pl} n_i^{pl}/n_a^{pl}$. The ionization coefficient, see Ref. [45],

$$\alpha_c = \frac{8\pi m_c}{(2\pi m_c k_B T)^{3/2}} \int_{I^{eff}}^{\infty} dE\, E\, \sigma_c^{ion}(E) e^{-E/k_B T}, \tag{11}$$

can be written in terms of the impact ionization cross section $\sigma_c^{ion}(E)$. There are several papers related to the vacuum impact ionization cross section, as well as the behavior near the shock wave front [46,47,52]. The ionization energy I^{eff} is modified by medium effects. The ionization potential depression was discussed recently [51] and leads to a significant change of the ionization coefficient under plasma conditions considered here. This was already shown by Bornath *et al.* [45], where the impact ionization cross sections was taken in Born approximation. Other effects which may influence the effective width of the plasma front layer are photo ionization turbulences and nonplanar interfaces, but have been excluded from considerations so far.

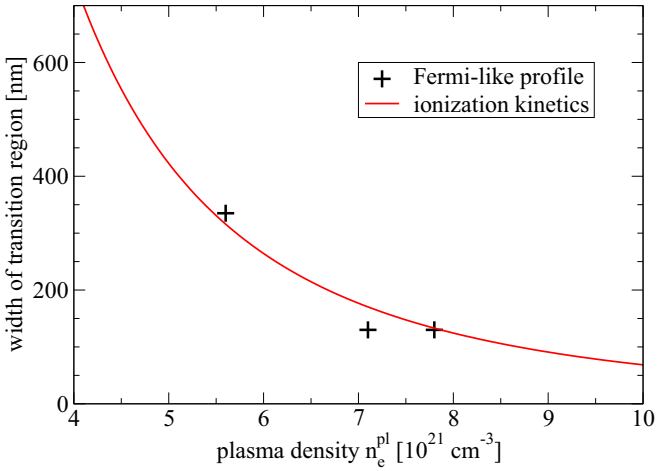

FIG. 12. Density dependence of the width of the shock wave front. Three data points derived from the Fermi-like profile, see Fig. 6, are compared to a preliminary curve derived from ionzation kinetics, see the Appendix

With a shock front velocity v and an ionization rate $(\alpha_e\, n_0)$, see Table I, the width of the shock front layer is approximately $d = v/(\alpha_e\, n_0)$. According to previous work [8,9,25], the shock wave velocity is in the order of 5 km/s. With an ionization rate of 10^{10} s^{-1}, we find a width of 500 nm. This is by a factor of 2 above the width obtained from fitting the experimentally observed reflectivities, see Fig. 6 and analysis in the text. In the Appendix, a simple model for the ionization kinetics has been considered to derive ionization rates specific to our experimental setup.

Experiments at different densities, as shown in Fig. 7, allow to investigate the dependence of the free-electron density profile as function of the density. In Fig. 12 we give the width d of the free-electron density profile derived from the experimental data compared to a general behavior obtained from the model of ionization kinetics, see the Appendix. Good agreement is achieved which supports our general model assumptions.

V. CONCLUSION

We obtain results for highly shock-compressed Xe plasmas obtained through laser diagnostics, measuring the reflectivity for different wavelengths and different incident angles. The dependence on the electron density is investigated. Experimental data in the region of very high temperatures and densities are difficult to obtain. However, they are very important for validating theoretical models and for fitting them to actually observed constraints.

We show that reflectivity measurement may be used to explore the free-electron density profile of the front layer of shock-wave produced plasmas. This is of relevance because often reflectivity measurements are used to infer the conductivity and other properties of shock-wave produced plasmas. Our calculations show that the Fresnel approximation does not describe the experiment satisfyingly, but the use of smooth charge particle profile describes the experimental data more

correctly. We assumed a Fermi-like free-electron density with three parameters to be optimized. This density profile depends on the plasma parameters n_e^{pl} and temperature T. Measurements of the reflectivity at different wavelengths of the laser diagnostics and for different polarizations and incident angles allow to infer the free-electron density profile $n_e(z)$. It is a confirmation of the model that the same profile (produced under the same experimental conditions) can explain the measured reflectivity data for arbitrary λ, θ, and polarization (s, p), including the Brewster angle. Also the theoretical approach to take into account different collisional processes is well established due to successful applications to the description of thermoelectric properties dense partially ionized plasmas, like Xenon and other inert gases as well as dense metal plasmas.

The comparison with theoretical calculations gives a thickness of the shock front sheet of about 200–290 nm. It decreases with increasing plasma density. These results are of relevance also for the interpretation of other reflectivity measurements to probe the properties of WDM, in particular, the metallization of hydrogen and other gases at high densities.

Theoretically, the formation of the plasma after the shock front must be considered as a dynamical process. Different processes, radiation as well as collisional, contribute to ionization near the shock wave front. Ionization kinetics can be used, and density effects are relevant for the ionization and recombination rates. The collisional part, assumed to be proportional to the density of the ion and atom components, is modified at high densities where screening and ionization potential depression become important. As a consequence, the profile is steeper at high densities, and the width of the front is larger at low densities. The experimental evaluation of the density profile allows to obtain information about microscopic processes in a region of strong nonequilibrium such as the shock front.

A kinetic approach to obtain the free-electron density profile is in progress. Because the densities are high, medium effects such as screening and ionization potential depression are of interest. In the opposite direction, these investigations may provide us with the possibility to investigate the microscopic processes, in particular ionization, in a dense medium, if the shock-front profile is measured.

ACKNOWLEDGMENTS

The authors thank V.K. Gryaznov for providing thermodynamic parameters for the new data points, obtained from the program package SAHA IV. The authors acknowledge financial support by DFG RE 975/4-1 & RO 905/32-1 and RFBR Grant No. 19-52-12039 for the collaborative project *Thermodynamical and optical properties of dense nobel gas plasma*.

APPENDIX: DENSITY PROFILE FROM IONIZATION KINETICS

In this Appendix we compare the Fermi-like profile (6), which was obtained by fitting to the experimental data, to results for a simple ionization kinetic model. Starting from the rate equation, Eq. (10), we restrict ourselves to the electronic contribution ($c = \mathrm{e}$)

$$\dot{n}_\mathrm{e}(t) = \alpha_\mathrm{e}\left\{\left[n_\mathrm{heavy}^\mathrm{pl} - n_\mathrm{e}(t)\right]n_\mathrm{e}(t) - bn_\mathrm{e}^3(t)\right\}, \tag{A1}$$

where the parameter $b = \beta_\mathrm{e}/\alpha_\mathrm{e}$ is determined by the stationary solution as $b = n_\mathrm{a}^\mathrm{pl}/(n_e^\mathrm{pl})^2$. The ionization coefficient α_e is treated as a free parameter.

Assuming a shock front velocity of $v = dz/dt$, we transform the rate equation with respect to time into a differential equation with respect to the position z with $\dot{n}_\mathrm{e}(t) = v\partial_z n_\mathrm{e}(z)$ for the electron density profile

$$\frac{dn_\mathrm{e}(z)}{dz} = \frac{\alpha_\mathrm{e}}{v}\left\{\left[n_\mathrm{heavy}^\mathrm{pl} - n_\mathrm{e}(z)\right]n_\mathrm{e}(z) - bn_\mathrm{e}^3(z)\right\}. \tag{A2}$$

This differential equation is unique up to a shift z_0 in the profile.

According to previous work [8,9,25], the shock wave velocity is in the order of $v = dz/dt = 5$ km/s. With this, fitting the solution of the ionization kinetic model (A2) to the Fermi-like profile, Eq. (6), we find an ionization coefficient of $\alpha_\mathrm{e} = 7.14 \times 10^{-18}\,\mathrm{m}^3/\mathrm{s}$ for the lower density $\rho = 1.8\,\mathrm{g/cm}^3$ and $\alpha_\mathrm{e} = 10.9 \times 10^{-18}\,\mathrm{m}^3/\mathrm{s}$ for the higher density $\rho = 2.8\,\mathrm{g/cm}^3$. The results are shown in Fig. 13.

The values of the ionization coefficients are of the same order as for hydrogen at 30 000 K if considering collisions

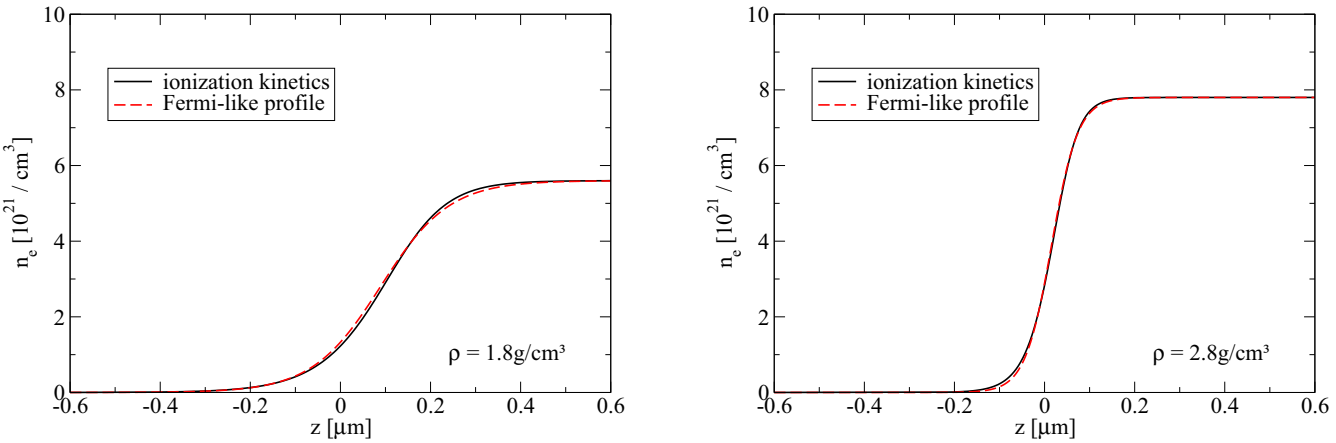

FIG. 13. Free electron density profiles described by the simple ionization kinetics model, Eq. (A2), (black, full line) in comparison to the Fermi-like profile, Eq. (6), (red, dashed line) for the plasma densities $\rho = 1.8\,\mathrm{g/cm}^3$ (left) and $\rho = 2.8\,\mathrm{g/cm}^3$ (right).

with electrons only. The value $\alpha_e = 78.8 \times 10^{-18}$ m^3/s was given in Ref. [45]. For collisions with neutral atoms the value is slightly smaller because of the short-range interaction. Still, our results are significantly lower. This may be explained by the fact that the temperature T_e of the electron subsystem remains below the plasma temperature T^{pl} as long as impact ionization occurs which reduces the thermal energy of the electron subsystem. Our inferred rates of impact ionization seem to be more consistent with a temperature T_e of about 20 000 K. The investigation of the nonequilibrium state in the plasma front layer where ionization processes occur needs more investigations including the concept of different temperatures for electrons and ions to be worked out in subsequent work.

To get an estimate for the width of the transition region in the shock wave front, see Fig. 12, we assume the following fits for the ionization degree $\alpha_{ion}(n^{pl}_{heavy}) = -0.136 \ln(n^{pl}_{heavy}[10^{21}/\mathrm{cm}^3]) + 0.956$ and ionization coefficient $\alpha_e(n^{pl}_{heavy}) = 0.170\, n^{pl}_{heavy}[10^{21}/\mathrm{cm}^3]$. The fit for the ionization degree is based on a regression of present and former calculations using the program package SAHA IV, see Ref. [10]. For the ionization coefficient, a linear interpolation of the fitted values is used. The profile width is shown in Fig. 12.

[1] G. W. Collins *et al.*, Contrib. Plasma Phys. **39**, 13 (1999).
[2] P. M. Celliers, G. W. Collins, L. B. DaSilva, D. M. Gold, R. Cauble, R. J. Wallace, M. E. Foord, and B. A. Hammel, Phys. Rev. Lett. **84**, 5564 (2000).
[3] P. Loubeyre *et al.*, High Pressure Res. **24**, 25 (2004).
[4] M. D. Knudson *et al.*, Science **348**, 1455 (2015).
[5] M. Zaghoo, A. Salamat, and I. F. Silvera, Phys. Rev. B **93**, 155128 (2016).
[6] C. Zha *et al.*, Phys. Rev. Lett. **119**, 075302 (2017).
[7] A. F. Goncharov and Z. M. Geballe, Phys. Rev. B **96**, 157101 (2017).
[8] V. B. Mintsev and Yu. B. Zaporoghets, Contrib. Plasma Phys. **29**, 493 (1989).
[9] H. Reinholz, Y. Zaporoghets, V. Mintsev, V. Fortov, I. Morozov, and G. Röpke, Phys. Rev. E **68**, 036403 (2003).
[10] Yu. Zaporozhets, V. Mintsev, V. Gryaznov, V. Fortov, H. Reinholz, T. Raitza, and G. Röpke, J. Phys. A: Math. Gen. **39**, 4329 (2006).
[11] Yu. B. Zaporozhets, V. B. Mintsev, V. K. Gryaznov, and V. E. Fortov, *Physics of Extreme States of Matter* 2002, edited by V. E. Fortov *et al.* Chernogolovka: IPCP RAS, 2002. p. 188. [in Russian].
[12] H. Reinholz, G. Röpke, I. Morozov, V. B. Mintsev, Yu. B. Zaporozhets, V. Fortov, and A. Wierling, J. Phys. A: Math. Gen. **36**, 5991 (2003).
[13] Yu. B. Zaporozhets, V. B. Mintsev, V. K. Gryaznov, V. E. Fortov, H. Reinholz, and G. Röpke, *Physics of Extreme States of Matter* 2004, edited by V. E. Fortov *et al.* Chernogolovka: IPCP RAS, 2004. p. 140. [in Russian].
[14] M. A. Berkovsky, Y. K. Kurilenkov, and H. M. Milchberg, Phys. Fluids B **4**, 2423 (1992).
[15] Y. K. Kurilenkov, M. A. Berkovsky, S. Hocini, and J. Skowronek, J. Phys. B: At. Mol. Opt. Phys. **28**, 2021 (1995).
[16] S. A. Magnitskiy, I. V. Morozov, G. E. Norman, and A. A. Valuev, J. Phys. A: Math. Gen. **36**, 5999 (2003).
[17] D. Ballester and I. M. Tkachenko, Contrib. Plasma Phys. **45**, 293 (2005).
[18] I. M. Tkachenko and D. Ballester, J. Phys.: Conf. Ser. **11**, 82 (2005).
[19] Desjarlais, Contrib. Plasma Phys. **45**, 300 (2005).
[20] P. A. Zhilyaev, G. E. Norman, I. M. Saitov, and V. V. Stegailov, Dokl. Phys. **58**, 277 (2013).
[21] G. Norman *et al.*, Contrib. Plasma Phys. **53**, 300 (2013).
[22] G. Norman, I. Saitov, V. Stegailov, and P. Zhilyaev, Phys. Rev. E **91**, 023105 (2015).
[23] G. Norman and I. Saitov, Phys. Rev. E **94**, 043202 (2016).
[24] H. Reinholz, G. Röpke, A. Wierling, V. B. Mintsev, and V. K. Gryaznov, Contrib. Plasma Phys. **43**, 3 (2003).
[25] Yu. B. Zaporozhets, V. B. Mintsev, V. K. Gryaznov, V. E. Fortov, H. Reinholz, and G. Röpke, J. Phys. A: Math. Theor. **42**, 214063 (2009).
[26] H. Reinholz, G. Röpke, S. Rosmej, and R. Redmer, Phys. Rev. E **91**, 043105 (2015).
[27] J. R. Adams, H. Reinholz, R. Redmer, V. B. Mintsev, N. S. Shilkin, and V. K. Gryaznov, Phys. Rev. E **76**, 036405 (2007).
[28] S. Rosmej, H. Reinholz, and G. Röpke, Phys. Rev. E **95**, 063208 (2017).
[29] W. Ebeling, A. Förster, V. Fortov, V. Gryaznov, and A. Polishchuk A, *Thermophysical Properties of Hot Dense Plasmas* (Teubner, Stuttgart, Germany, 1991).
[30] V. E. Fortov, V. K. Gryaznov, V. B. Mintsev, V. Ya. Ternovoi, I. L. Iosilevskiy, M. V. Zhernokletov, and M. A. Mochalov, Contrib. Plasma Phys. **41**, 215 (2001).
[31] V. E. Fortov *et al.*, JETP **97**, 259 (2003).
[32] V. K. Gryaznov, I. L. Iosilevskiy, and V. E. Fortov, AIP Conf. Proc. **1426**, 917 (2012).
[33] H. Reinholz, R. Redmer, G. Röpke, and A. Wierling, Phys. Rev. E **62**, 5648 (2000).
[34] S. Rosmej, Contrib. Plasma Phys. **56**, 327 (2016).
[35] W.-D. Kraeft, D. Kremp, W. Ebeling, and G. Röpke, *Quantum Statistics of Charged Particle Systems* (Plenum, New York, 1986).
[36] Yu. B. Zaporozhets, Y. A. Omarbakiyeva, H. Reinholz, G. Röpke, V. B. Mintsev, and V. K. Gryaznov, Contr. Plasma Phys. **56**, 467 (2016).
[37] E. O. Shalenov *et al.*, Contrib. Plasma Phys. **57**, 486 (2017).
[38] S. Udrea, N. Shilkin, V. E. Fortov, D. H. H. Hoffmann, J. Jacoby, M. I. Kulish, V. B. Mintsev, P. Ni, D. Nikolaev, N. A. Tahir, and D. Varentsov, J. Phys. A: Math. Gen. **39**, 4743 (2006).
[39] T. Raitza, H. Reinholz, G. Röpke, V. Mintsev, and A. Wierling, J. Phys. A: Math. Gen. **39**, 4393 (2006).
[40] M. E. Dieckmann, H. Ahmed, G. Sarri, D. Doria, I. Kourakis, L. Romagnani, M. Pohl, and M. Borghesi, Phys. Plasmas **20**, 042111 (2013).

[41] Ya. B. Zeldovich and Y. P. Raizer *Physics of Shock Waves, and High-Temperature Hydrodynamic Phenomena* Vol. 1, edited by W. D. Hayes and R. F. Probstein (Academic, New York, 1966).
[42] H. Petschek and S. Byron, Ann. Phys. (NY) **1**, 270 (1957).
[43] L. M. Biberman, V. S. Vorob'ev, and I. T. Yakubov, *Kinetics of Nonequilibrium Low-Temperature Plasmas* (Nauka, Moscow 1982, and Consultants Bureau, NY 1987).
[44] V. Shanmugasundaram and S. S. R. Murty, J. Plasma Phys. **20**, 419 (1978).
[45] M. Schlanges and Th. Bornath, Physica A **192**, 262 (1993).
[46] V. Aslanyan and G. J. Tallents, Phys. Rev. E **91**, 063106 (2015).
[47] Z. Q. Wu *et al.*, J. Phys. B: At. Mol. Opt. Phys. **35**, 2305 (2002).
[48] T. J. McIntyre, A. F. P. Houwing, R. J. Sandeman, and H.-A. Bachor, J. Fluid Mech. **227**, 617 (1991).
[49] H. Ezumi *et al.*, J. Phys. Soc. Jpn. **43**, 1060 (1977).
[50] Y. Takano and T. Akamatsu, Z. Naturforsch. **32 a**, 986 (1977).
[51] C. Lin, G. Röpke, W. D. Kraeft, and H. Reinholz, Phys. Rev. E **96**, 013202 (2017).
[52] M. G. Kapper and J.-L. Cambier, J. Appl. Phys. **109**, 113308 (2011).